Haldane model with chiral edge states using a synthetic dimension

Joel Priestley,* Gerard Valentí-Rojas, and Patrik Öhberg
SUPA, Institute of Photonics and Quantum Sciences, Heriot-Watt University, Edinburgh EH14 4AS, United Kingdom

(Received 30 June 2023; revised 2 October 2023; accepted 10 January 2024; published 20 February 2024)

We explicitly show that the differences, with respect to the appearance of topological phases, between the traditional Haldane model, which utilizes a honeycomb lattice structure, and the Haldane model imbued onto a brick-wall lattice geometry are inconsequential. A proposal is then put forward to realize the Haldane model by exploiting the internal degrees of freedom of atoms as a synthetic dimension. This leads to a convenient platform for the investigation of chiral edge states due to the hard boundaries provided by the hyperfine manifold. We make some cursory comments on the effects of interactions in the system.

DOI: 10.1103/PhysRevA.109.023322

I. INTRODUCTION

Haldane's work from 1988 using a "toy" model demonstrated how a nonzero band Chern number, and therefore a nonzero quantized Hall conductance, could be achieved in "2D graphite" with a net-zero magnetic field [1]. In that article Haldane expressed doubts about whether the model is physically realizable, yet some 20 years later it was experimentally achieved in an ultracold Fermi gas [2]. Two of the main signatures of topological phases of matter are edge states and a quantized Hall conductance. Both of these hallmarks were previously observed in synthetic-dimensional systems in a quantum Hall regime [3,4].

In recent years there has been growing interest in synthetic dimensions where, for example, the states of the hyperfine manifold of an atom are coherently coupled together, allowing for the construction of a $(D+1)$-dimensional system from one which has D spatial dimensions [5]. This new method has come with its own plaudits, and schemes have been proposed which would realize topological states of matter such as the four-dimensional quantum Hall effect [6] and even the six-dimensional quantum Hall effect [7,8], as well as more exotic physics such as the Creutz-Hubbard model [9]. Using synthetic gauge fields, high effective magnetic field strengths, otherwise experimentally unattainable, have been realized in ultracold atoms to simulate the Harper-Hofstadter model, having an important bearing in the realization of topological phases [10,11]. Here, Raman-assisted tunneling was utilized, and proposals have also been put forward to realize the anyonic Bose-Hubbard model using this technique [12]. In this work, we propose an experimental scheme using synthetic dimensions to attain the Haldane model on a bipartite brick-wall lattice with complex next-nearest-neighbor tunneling.

First, we analyze the differences between the Haldane model on its traditional honeycomb lattice and on a brick-wall lattice to ensure the system retains the desired properties. Next, we propose using a synthetic dimension to create the Haldane model, achieved by the use of Raman-assisted tunneling, which can imprint complex phases on the wave function of the atom. In implementing this, one would capture the spirit of Haldane's proposal to generate a nonzero Hall conductance without the appearance of Landau levels. One advantage of using such a synthetic dimension is the hard boundaries. The hyperfine manifold provides an ideal platform for the investigation of chiral edge states [13], as opposed to the case with degenerate atomic gases, in which the edge of the sample is usually imposed gradually by harmonic confinement and which thus do not reflect an abrupt termination such as that found on a sample of graphene. The edge-state physics is therefore nontrivial and needs to be considered in its own right [14,15]. Floquet techniques allow for the creation of real-space edge states in optical lattices with ultracold atoms. This was achieved by illuminating a region of the condensate in the lattice with a repulsive optical potential, thus creating a hard boundary [16]. Synthetic dimensions built from the hyperfine manifold have the advantage that they are manipulated optically, leading to high controllability and flexibility.

According to the bulk-boundary correspondence [17,18], for a nonzero Chern number one expects to observe edge states, and previous studies predicted their existence for the specific case of the Haldane model [19]. Previously, to identify the topological nature of the Haldane model [2], a constant force was applied, and this resulted in an observed, orthogonal drift. This drift is analogous to a Hall current. The topology of the band can be explored by inducing Bloch oscillations and mapping out in quasimomentum space the locations of the Dirac points [2]. Chiral edge states in experimental analogs of graphene have been observed in photonic lattice systems [20]. Edge states in synthetic-dimensional systems were previously reported, and the way in which they were detected,

*jcp2@hw.ac.uk

TABLE I. Summary of differences between the honeycomb and brick-wall lattice Haldane models.

Lattice property	Honeycomb	Brick wall (six next-nearest neighbors)
Nearest neighbor	$\mathbf{a_1} = \begin{pmatrix} \frac{1}{2} \\ \frac{\sqrt{3}}{2} \end{pmatrix} a$, $\mathbf{a_2} = \begin{pmatrix} -\frac{1}{2} \\ \frac{\sqrt{3}}{2} \end{pmatrix} a$, $\mathbf{a_3} = \begin{pmatrix} 0 \\ -1 \end{pmatrix} a$	$\mathbf{a_1} = \begin{pmatrix} 1 \\ 0 \end{pmatrix} a$, $\mathbf{a_2} = \begin{pmatrix} -1 \\ 0 \end{pmatrix} a$, $\mathbf{a_3} = \begin{pmatrix} 0 \\ -1 \end{pmatrix} a$
Next-nearest neighbor	$\mathbf{b_1} = (\mathbf{a}_2 - \mathbf{a}_3)$, $\mathbf{b_2} = (\mathbf{a}_3 - \mathbf{a}_1)$, $\mathbf{b_3} = (\mathbf{a}_1 - \mathbf{a}_2)$	$\mathbf{b_1} = (\mathbf{a}_2 - \mathbf{a}_3)$, $\mathbf{b_2} = (\mathbf{a}_3 - \mathbf{a}_1)$, $\mathbf{b_3} = (\mathbf{a}_1 - \mathbf{a}_2)$
Flux	$\phi = \frac{2\pi(2\Phi_a + \Phi_b)}{\Phi_0}$	$\phi = \frac{2\pi(\Phi_a + \Phi_b)}{\Phi_0}$
Brillouin zone	Hexagon	$\frac{\pi}{4}$ rotated square
Dirac points	$M = \pm 3\sqrt{3}\, t_2 \sin\phi$	$M = \pm 3\sqrt{3}\, t_2 \sin\phi$

using spin-selective imaging, is a valuable experimental asset [3,4].

A proposal for an experiment to simulate generalized Wilson-Dirac fermions, where Haldane-like phases surprisingly appear, has already been proposed [21]. However, there are fundamental differences between our proposals and [21]. Primarily, [21] uses only two internal states and therefore has no synthetic-dimensional "bulk," whereas our proposal may be extended to an arbitrary number of states of the hyperfine manifold. This allows for a larger bulk within the synthetic lattice, which is especially useful for the comparison of bulk states to chiral edge states. We envision probing these states by way of spin-selective imaging, whereas no experimental process for the isolation and measurement of either type of state is included in [21]. We also discuss the role of anisotropy and the number of nearest-neighbor couplings required to see the classical Haldane phase diagram, as this is especially pertinent information if one wishes to simulate the Haldane model by forming a synthetic lattice as we propose. The other main distinction between our work and [21] is that through derivation we arrive specifically at the Haldane Hamiltonian from a laboratory Hamiltonian, with complex tunneling terms associated with next-nearest-neighbor couplings as opposed to nearest-neighbor tunnelings as in [21]. As a result, the topological phases have no dependency on the modulus of the complex hopping rates, a characteristic which is not seen in the original Haldane model or our proposal. Finally, our work in conjunction with [21] demonstrates ways in which to investigate physics involving Majorana fermions [22] and parafermions [23] due to the close relationships that these models have.

This article is structured as follows: In Sec. II we analyze the effects of deforming the lattice from a honeycomb to a brick-wall lattice. In Secs. III and IV, we put forward our experimental proposal for the Haldane model. Section V focuses on the much-sought-after edge states. Section VI discusses the effects of interactions. We conclude with a summary of our proposal and outlook for Chern insulators in synthetic-dimensional systems in Sec. VII.

II. THE BRICK-WALL HALDANE MODEL

The Haldane model [1] fundamentally relies on the breaking of two symmetries. The first is inversion symmetry, accomplished by breaking the sublattice symmetry. Mathematically, this is represented by an energy offset $\pm M$ between neighboring sites, labeled A and B, respectively. The second symmetry is time-reversal symmetry. This is broken by the introduction of complex next-nearest-neighbor tunneling, which involves the accumulation of a phase. This can be viewed as a Peierls phase or flux through a plaquette. The competition between these two broken symmetries determines which phase the system is in. The eigenvector of a bipartite Hamiltonian, written in Bloch form, is a two-vector whose elements are the wave functions on the A and B sites. The Haldane model Bloch Hamiltonian is given by

$$\hat{\mathbf{H}} = \sum_{\mathbf{k}} \hat{\boldsymbol{\Psi}}^{\dagger}(\mathbf{k}) \hat{\mathcal{H}}(\mathbf{k}) \hat{\boldsymbol{\Psi}}(\mathbf{k}), \tag{1}$$

with

$$\hat{\mathcal{H}}(\mathbf{k}) = 2t_2 \cos\phi \left[\sum_i \cos(\mathbf{k}\cdot\mathbf{b}_i) \right] \mathbf{I} + t_1 \left(\sum_i [\cos(\mathbf{k}\cdot\mathbf{a}_i)\sigma_x + \sin(\mathbf{k}\cdot\mathbf{a}_i)\sigma_y] \right) + \left\{ M - 2t_2 \sin\phi \left[\sum_i \sin(\mathbf{k}\cdot\mathbf{b}_i) \right] \right\} \sigma_z, \tag{2}$$

where $\hat{\boldsymbol{\Psi}}(\mathbf{k}) = (\hat{\psi}_A, \hat{\psi}_B)^{\top}$ is the Bloch state spinor. This form of the Hamiltonian is general; no choice of geometry has yet been made, which is enforced by the input of specific vectors $\mathbf{a}_i$ and $\mathbf{b}_i$ as the arguments of the trigonometric functions. Notationwise, t_1 is the real nearest-neighbor tunneling probability, t_2 is the modulus of the next-nearest-neighbor tunneling probability, and ϕ is the phase gain associated with next-nearest-neighbor hopping, mathematically originating from the argument of the next-nearest-neighbor tunneling. Moreover, $\mathbf{a}_i$ and $\mathbf{b}_i$ are the spatial vectors of nearest and next-nearest neighbors, respectively, and $\sigma_{x,y,z}$ are the Pauli matrices. The spatial vectors from a B site to a nearest-neighbor A site for the honeycomb lattice are $\mathbf{a}_1 = (\frac{a}{2}, \frac{\sqrt{3}a}{2})^{\top}$, $\mathbf{a}_2 = (-\frac{a}{2}, \frac{\sqrt{3}a}{2})^{\top}$, and $\mathbf{a}_3 = (0, -a)^{\top}$, and the next-nearest-neighbor vectors are consequently given by $\mathbf{b}_1 = \mathbf{a}_2 - \mathbf{a}_3$, $\mathbf{b}_2 = \mathbf{a}_3 - \mathbf{a}_1$, and $\mathbf{b}_3 = \mathbf{a}_1 - \mathbf{a}_2$ (see Fig. 1). The brick-wall lattice vectors are given by $\mathbf{a}_1 = (a, 0)^{\top}$, $\mathbf{a}_2 = (-a, 0)^{\top}$, and $\mathbf{a}_3 = (0, -a)^{\top}$, and the next-nearest-neighbor displacements are as above. In both cases a is the lattice spacing, that is, the shortest distance between any two sites. To break time-reversal symmetry, phase gain is only positive from next-nearest-neighbor hopping in a clockwise

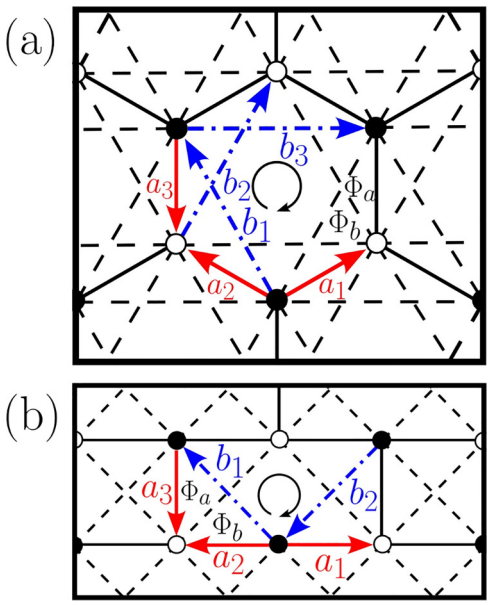

FIG. 1. Nearest neighbors are connected to one another by the vectors $\pm\mathbf{a_1}, \pm\mathbf{a_2}$, and $\pm\mathbf{a_3}$, and hopping between these sites occurs at a rate t_1. Next-nearest neighbors are reached by the vectors $\pm\mathbf{b_1}, \pm\mathbf{b_2}$, and $\pm\mathbf{b_3}$, and this occurs at a rate t_2 and comes with a phase gain ϕ. The direction of an arrow indicates positive phase gain. Fluxes through regions divided by the hoppings have been labeled. The phase gained by traversing around an entire plaquette is equivalent to the enclosed flux and hence is $2\Phi_a + \Phi_b$ in the honeycomb case and $\Phi_a + \Phi_b$ in the brick-wall case. (a) A honeycomb lattice with all couplings indicated in black, with dashed lines for next-nearest-neighbor vectors; again, arrows show the direction of positive phase gain. The A and B sites are represented by white and black dots, respectively. Superimposed solid red arrows represent the nearest-neighbor vectors, while blue dot-dashed arrows represent next-nearest-neighbor lattice vectors. (b) Brick-wall lattice; conventions are the same as in (a). We now see explicitly that nearest-neighbor lattice vectors a_1 and a_2 are no longer linearly independent. See Table I for mathematical definitions of these vectors.

circulation, as shown in Fig. 1. The Hamiltonian (2) can be put in the form

$$\hat{\mathcal{H}}(\mathbf{k}) = \varepsilon(\mathbf{k})\mathbf{I} + \mathbf{d}(\mathbf{k}) \cdot \sigma, \tag{3}$$

with σ being the Pauli vector, and the spectrum is given by

$$E_{\pm}(\mathbf{k}) = \varepsilon(\mathbf{k}) \pm \sqrt{\mathbf{d}(\mathbf{k}) \cdot \mathbf{d}(\mathbf{k})}, \tag{4}$$

where $\mathbf{d}(\mathbf{k})$ are the coefficients of the Pauli matrices. By first defining the unit vector of these coefficients

$$\mathbf{n}(\mathbf{k}) = \frac{\mathbf{d}(\mathbf{k})}{|\mathbf{d}(\mathbf{k})|}, \tag{5}$$

one can calculate the topological invariant of an insulator with broken time-reversal symmetry, the first Chern number. The Chern number is related to the solid angle, which is subtended by the unit vector $\mathbf{n}(\mathbf{k})$ in $\mathbf{k}$ space as $\mathbf{k}$ runs over the Brillouin zone. Therefore, for the lower band this can be found with [24]

$$\nu_1 = -\frac{1}{4\pi} \iint_{\mathrm{BZ}} d^2k \; \mathbf{n} \cdot [(\partial_{k_x}\mathbf{n}) \times (\partial_{k_y}\mathbf{n})], \tag{6}$$

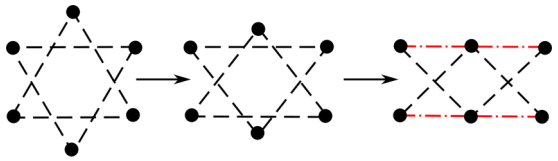

FIG. 2. Deformation of the honeycomb lattice to brick-wall lattice geometry; for demonstrative purposes only next-nearest-neighbor links are shown. Red links (the parallel top and bottom dot-dashed lines) are the next-nearest-neighbor couplings that we consider dropping since they align with nearest-neighbor couplings which enclose no flux.

where the integrand is known as the Berry curvature and the integral is over the first Brillouin zone. Then, the Hall conductance of the system is given by

$$\sigma_{xy} = \nu_1 \frac{e^2}{h}, \tag{7}$$

despite the net magnetic field $\mathbf{B} = \mathbf{0}$. The Haldane model is therefore a topological insulator.

The brick-wall lattice is topologically equivalent to the honeycomb lattice. One could imagine smoothly deforming the honeycomb lattice by flattening out the top and bottom points of the hexagon. The Dirac points, if the system is in a regime in which these points exist, move away from the boundary of the Brillouin zone at $\mathbf{K} = \frac{2\pi}{3a}(1, \frac{1}{\sqrt{3}})^\top$ and $\mathbf{K}' = \frac{2\pi}{3a}(1, -\frac{1}{\sqrt{3}})^\top$ to two points deeper within the now square Brillouin zone at $(\pm\frac{2\pi}{3a}, 0)^\top$. The honeycomb lattice with three nearest neighbors has six next-nearest neighbors. It is not unreasonable to consider that the next-nearest-neighbor hoppings which go along the long side of the real-space lattice in the brick-wall case can be dropped (see Fig. 2) as the sites which these tunnelings connect move away from one another. By "straightening out" the lattice in this way, one adiabatically deforms the model into a relatively simpler one. Along this deformation path the system remains gapped since the Hamiltonian depends linearly on t_1 and the other hopping terms are robust against this deformation. There are therefore two options in the brick-wall case, six or four next-nearest neighbors.

To ensure that no relevant physics is lost by changing the lattice from a honeycomb to a brick-wall lattice, the Chern number as a function of phase and M/t_2 is calculated numerically (see Fig. 3). The six-next-nearest-neighbor brick-wall- and honeycomb-lattice situations are identical. In the four-next-nearest-neighbor brick-wall system, the boundaries of the phases, i.e., the lines in parameter space where the phase transition occurs, are moved relative to the six-next-nearest-neighbor case. A phase transition occurs when a band gap closes, and at this Dirac point, nontrivial topology in the form of Berry curvature is introduced to the band structure. Since these Dirac points are a point of degeneracy in the spectrum, they can easily be calculated using Eq. (4) by finding the points in reciprocal space for which $\mathbf{d}(\mathbf{k}) = 0$. This leads to boundaries defined by $\frac{M}{t_2} = \pm 3\sqrt{3}\sin\phi$ for the honeycomb and six-next-nearest-neighbor brick-wall lattice models and $\frac{M}{t_2} = \pm 2\sqrt{3}\sin\phi$ for the four-next-nearest-neighbor brick-wall case. It is instructive to verify that the physics remains

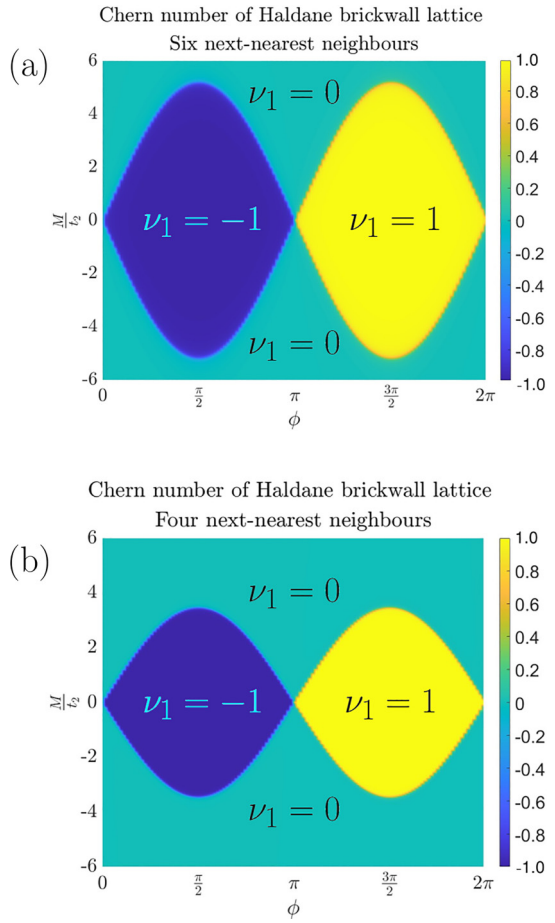

FIG. 3. The different phases have been labeled within the diagram with their Chern numbers ν_1. (a) The phase diagram for the honeycomb lattice. The six-next-nearest-neighbor brick wall gives the same plot. (b) The four-next-nearest-neighbor brick-wall lattice retains the same features but with a reduced area in parameter space for a topologically nontrivial band structure.

invariant, even though the lattice is deformed topologically, since there are additional symmetries that are broken. The honeycomb lattice enjoys a sixfold rotational symmetry which is reduced to a threefold one with the introduction of an energy offset, distinguishing every other site. The brick-wall lattice, however, has a twofold rotational symmetry which is reduced to the trivial group; that is, it only contains the identity when $M \neq 0$. As can be seen from the phase diagrams in Fig. 3, even for $M = 0$ the system is in a topological regime, $\phi \neq 0, \pi$, with $\nu_1 = \pm 1$ depending on the flux. A summary of the differences between the honeycomb- and brick-wall-lattice Haldane models is given in Table I.

Anisotropy

Next, we investigate the effect of anisotropy in the coupling constants of the model. We focus on the brick-wall four-next-nearest-neighbor case. This is a suitable candidate for our proposal since it requires fewer lasers since they correspond to next-nearest-neighbor hoppings. One can introduce directional anisotropy by setting the coupling along the y axis to $J_y = \xi t_1$ and the coupling along the x axis to $J_x = t_1$ and then

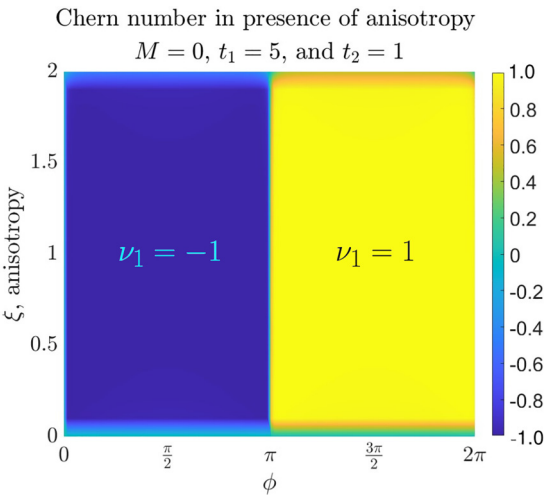

FIG. 4. Phase diagram for anisotropy in next-nearest-neighbor tunneling versus phase gain, with fixed on-site energy difference $M = 0$.

by varying ξ between 0 and 2 to investigate the effect of the topological phases due to the unequal coupling constants.

For three different M values, $M = 0$, 1, and 2, we plot anisotropy against flux in Figs. 4–6, respectively. We see that as the ratio of couplings increases, for $M \neq 0$, the range of phase with nontrivial topology gradually disappears and then is destroyed altogether, and the point at which this happens is different in all three cases. The regimes in these diagrams where the Chern number vanish correspond to a gapped trivial phase.

We see from Figs. 4–6 that even in the presence of anisotropy, nontrivial topology may still arise. This is more likely experimentally attainable. As can be seen from Fig. 6, if $J_y/J_x = \xi < 2$, then the nonzero Chern numbers remain. Anisotropy was previously shown to affect the appearance of edge states in graphene. At the same critical point as we find in Fig. 6, $J_y = 2J_x$, edge states on the zigzag edge were destroyed

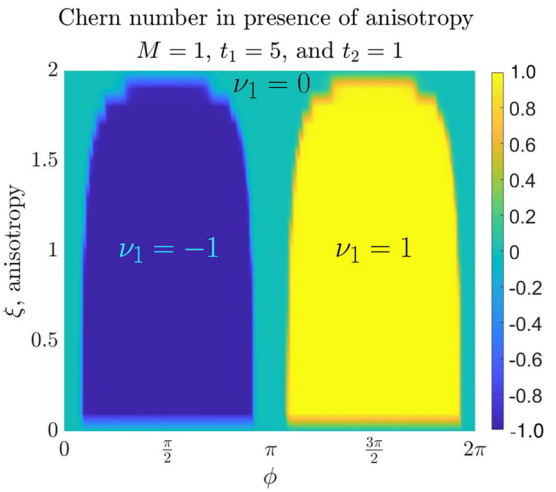

FIG. 5. Phase diagram for anisotropy in next-nearest-neighbor tunneling versus phase gain, with fixed on-site energy difference $M = 1$.

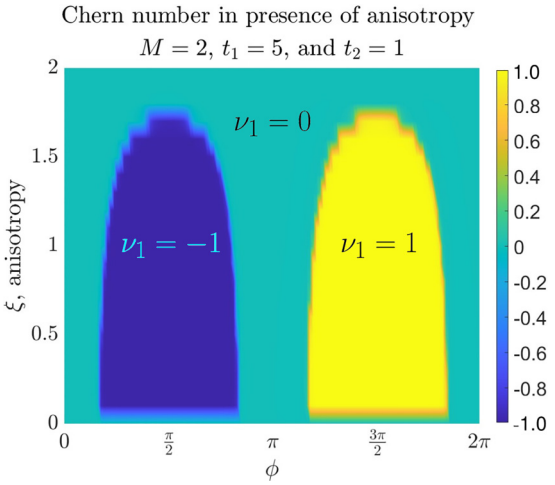

FIG. 6. Phase diagram for anisotropy in next-nearest-neighbor tunneling versus phase gain, with fixed on-site energy difference $M = 2$.

due to the merging of Dirac points, annihilating each other and removing the Berry curvature from the bands [18,25].

III. SYNTHETIC BRICK-WALL LATTICE

A. From laboratory to target Hamiltonian

Our proposal has two coupled dimensions, one of which is real and one of which is a synthetic dimension constructed from the internal states of the atoms, collectively known as the hyperfine manifold (Fig. 7). We begin by first constructing a brick-wall lattice, which as previously discussed will be the analog honeycomb lattice. This is done using an optical superlattice and Raman-assisted tunneling, with the result being Fig. 8. In the real dimension, which we take to be orientated along the x axis, there is an optical lattice within which resides a species of atom. The optical lattice is constructed using counterpropagating laser beams, and we assume strong

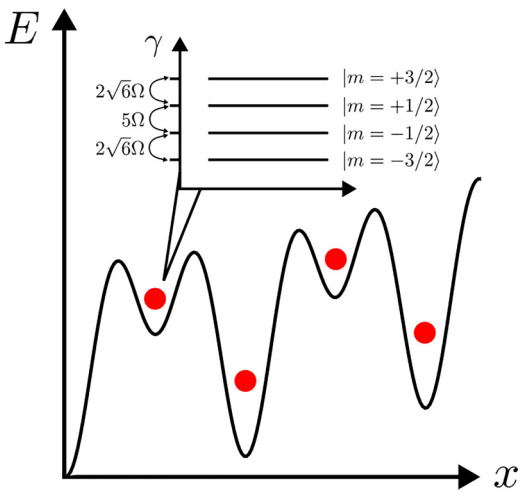

FIG. 7. Schematic diagram of the system. Red dots represent atoms, and the internal states (inset) used as an example are the four lowest spin-projection hyperfine states from a $F = 9/2$ manifold.

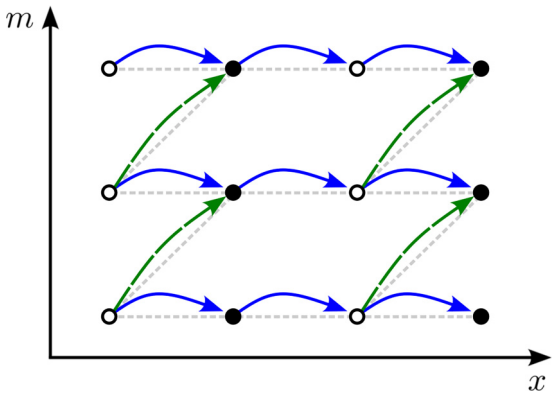

FIG. 8. Synthetic-dimensional brick-wall lattice structure, formed by the internal states of the atoms and a one-dimensional spatial lattice by way of Raman-assisted tunneling. The dotted lines are included to help illustrate the brick-wall structure. Here, m is an index that indicates the internal state, x represents the real-spatial-dimension direction, which is taken to be the x axis. Blue arrows (with solid tails) are hoppings purely along the real dimension, while green arrows (with long-dashed tails) are simultaneous transitions along real and synthetic dimensions.

confinement along other axes, thus limiting real-space dynamics to along the direction of beam propagation. A linear potential with amplitude $F > 0$ is applied to the lattice, which induces a tilt in energy along the x axis. This creates a laboratory Hamiltonian known as the Wannier-Stark Hamiltonian,

$$\hat{H}_{\mathrm{WS}} = \frac{\hat{p}^2}{2m} + V\cos^2(k_L\hat{x}) + F\hat{x}, \tag{8}$$

where V is the lattice depth and k_L is the wave vector of the lattice lasers. Next, we add to (8) a second potential with half the wavelength, which makes the lattice bipartite, and therefore, the beams form an optical superlattice. The sublattice sites will be denoted here by A and B. Hence, we obtain the Wannier-Stark superlattice Hamiltonian,

$$\hat{H}_{\text{WS-SL}} = \frac{\hat{p}^2}{2m} + V\cos^2(k_L\hat{x}) + U\cos^2(2k_L\hat{x}) + F\hat{x}. \tag{9}$$

In the second-quantized formalism, taking the reasonable approximation of considering only nearest-neighbor terms, this becomes

$$\hat{H}_{\mathrm{TB}} = \sum_j (\epsilon_j + aFj)\hat{a}_j^\dagger\hat{a}_j + \sum_j t_1(\hat{a}_{j+1}^\dagger\hat{a}_j + \hat{a}_j^\dagger\hat{a}_{j+1}), \tag{10}$$

where ϵ_j is of the form

$$\epsilon_j = E + V + \tfrac{1}{2}[1 + (-1)^j]U, \tag{11}$$

with the optical lattice inherently introducing an energy difference of U between adjacent sites. The energies in (11) stem from on-site integrals of the corresponding mode functions and will, to leading order, depend quadratically on their width relative to the lattice spacing. The above Hamiltonian is applicable for any internal state provided that the atom can be coupled to an adjacent site via some assisted-tunneling

scheme. For now we are only considering sites in the physical lattice, labeled by j. We have used, in reaching the final line of Eq. (11), $k_L = \frac{\pi}{a}$ and

$$E = -\frac{\hbar^2}{2m}\int_{-\infty}^{\infty} dx\ \psi_j^\dagger(x)\partial_x^2\psi_j(x), \tag{12}$$

where $\psi_j(x)$ is the Wannier function on site j. The Wannier functions are constructed from the Bloch functions and form a basis of states which are exponentially localized to the physical sites [26]

$$\psi_j(x) = \int_{-\pi/2}^{\pi/2} dk\ e^{-ikja}\phi_k(x), \tag{13}$$

where $\phi_k(x)$ is the Bloch function with quasimomentum k.

The linear potential $F\hat{x}$ inhibits the tunneling of atoms between neighboring sites. Nearest-neighbor hopping is reintroduced by the use of Raman-assisted tunneling. This is where two states are coupled together via an intermediary state, the ancillary state, by laser transitions. The net change in energy caused by such a process can be made equal to the energy difference between sites, and thus particle hopping is induced. This process will be discussed further in Sec. IV. This prevention and then reintroduction are required because additional control is necessary with regard to the hopping rates for our proposal. Using Raman-assisted tunneling, a complex phase can be imbued on the atom by having the laser beam incident on the optical lattice at an angle, which imparts a Raman recoil momentum along the x direction, for which we use the notation q_x, so the hopping integral below is multiplied by a factor e^{-ijq_x}.

The tunneling rate induced by the Raman-assisted tunneling for nearest neighbors along the x axis is given by [11,26,27]

$$t_{j\to j+1} = \Omega e^{-ijq_x}\int dx\ W_0(x)W_1(x)e^{-iq_x x}, \tag{14}$$

where j is a physical site index and $W_j(x)$ is the real-valued Wannier-Stark function (see Ref. [26]), which is the exact solution to (10), at site j. Hence, we identify $t_{j\to j+1}$ with t_1 in Eq. (10), but we require $q_x = 0$ as these will be nearest-neighbor hoppings when we go to form the Haldane model. The effective Rabi frequency Ω is given by [26]

$$\Omega = \frac{\Omega_{12}\Omega_{23}}{4\delta}, \tag{15}$$

where Ω_{12} is the one-photon Rabi frequency of a Raman beam which couples state 1 to an ancillary state 2, up to a detuning denoted by δ. Similarly, Ω_{23} is the one-photon Rabi frequency which couples state 3 to the ancillary state 2. Rabi frequencies will be discussed in further detail in Sec. IV. For now, one only needs to know that if atoms in site j are incident with laser light with frequencies Ω_{12} and Ω_{23}, then they will tunnel to a state $j+1$ at a rate $t_{j\to j+1}$ due to Eq. (14).

In the tight-binding model described thus far, the atoms are required to reside on the lowest rung of what is known as the Wannier-Stark ladder. This is a requirement because an atom in an excited Wannier-Stark state may tunnel to the ground state of an adjacent site.

The internal states of the atom can also be coupled together by the use of Raman beams or by the use of a radio-frequency magnetic field [4]. This forms a second dimension if one interprets each internal state as a different site. Using Raman-assisted tunneling, nearest-neighbor and next-nearest-neighbor hoppings in real-space were experimentally achieved [2,11], and for internal states their implementation was outlined in [5]. The double hopping in real space is achieved by tuning the effective Raman frequency to a frequency which is simply twice that required for a single hop [11].

As can be seen from Eq. (14), the phase gain is site dependent. The phase imprinted on the wave function allows for the engineering of a synthetic magnetic flux through a synthetic-dimensional "plaquette" which these complex hoppings bound [13]. Transitions along both real and synthetic dimensions, $(j, m) \to (j+1, m+1)$, can be induced simultaneously [26], and as will be shown below, due to the "geometry" of couplings that will be used, this will be a requirement. This is also governed by Eq. (14); however, the requisite polarizations of one of the Raman beams in this instance will be different.

Hence, we have three processes: Hopping along the superlattice, transitions between internal states, and the simultaneous occurrence of these two processes, which we shall refer to as the "diagonal" process. Using the latter two of these processes, a synthetic-dimensional lattice with diagonal tunnelings, resembling a rhombus, may be formed. From here one may create a brick-wall lattice with the inclusion of one extra step; one must remove every other diagonal hopping element. This is done by the introduction of an additional pair of lasers which also generate diagonal tunnelings. These lasers are then tuned such that they destructively interfere with the original diagonal Raman lasers on alternate sites. Equivalently, they will constructively interfere on alternating sites too. A relative phase may need to be introduced between the beams, and due to different operating frequencies, these lasers may also need to be coherently coupled to each other, for example, by a locking process by way of a frequency comb. Additionally, it should be noted that this effect only occurs if the Raman processes have the same amplitudes. See Fig. 8 for the resulting semisynthetic lattice, a lattice in both real and synthetic spaces, where blue arrows indicate tunneling purely in real space, i.e., hopping along the optical lattice, and green arrows represent the diagonal process, which is absent on every other site. The scheme for a brick-wall lattice described thus far is from Ref. [26].

We go one step further and propose that by starting from this brick-wall structure with all hopping terms phaseless and adding complex next-nearest-neighbor terms, one can achieve the Haldane model. To do this we will include next-nearest-neighbor terms in the second-quantized formalism of Eq. (10) by adding next-nearest hopping terms due to Raman-assisted tunneling. We will use the four-next-nearest-neighbor case to simplify proceedings.

We start now from Eq. (10). To distinguish the different hopping terms that will arise, we momentarily set $t_1 = J_x$, and we add an additional label, m, which will refer to the internal

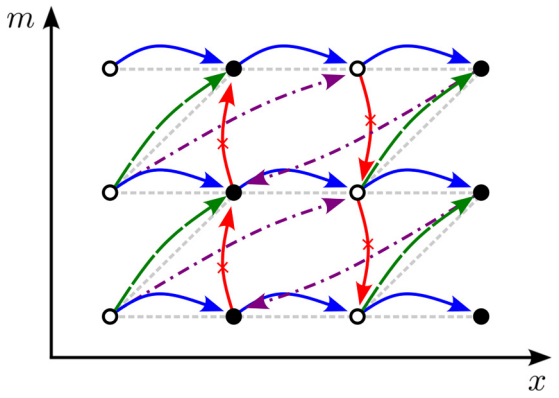

FIG. 9. Brick-wall lattice structure, with the same conventions as in Fig. 8, now with next-nearest-neighbor tunneling. White (black) dots represent the A (B) sites, made distinct by an energy offset. Red arrows (vertical and marked with a cross) are purely synthetic, and here, one sees that these arrows skip a site located at $(j-1,m)$. Hence, this transition is, in fact, a next-nearest-neighbor hopping. Purple arrows (dot-dashed tails) are the long-diagonal next-nearest-neighbor hopping. The direction of an arrow indicates positive phase gain.

state of an atom within the superlattice (9),

$$\hat{H}_{\mathrm{TB}} = \sum_{j}(\epsilon_{j,m} + aFj)\hat{a}^{\dagger}_{j,m}\hat{a}_{j,m} + \sum_{j} J_x(\hat{a}^{\dagger}_{j+1,m}\hat{a}_{j,m} + \hat{a}^{\dagger}_{j,m}\hat{a}_{j+1,m}). \tag{16}$$

The process to construct the nearest-neighbor hoppings is exactly the same as discussed thus far for the synthetic-dimensional brick-wall lattice. However, we have yet to include an explicit diagonal hopping term in our Hamiltonian (10). We will denote the contribution from the Raman laser for a diagonal process as $\hat{H}_{\mathrm{Diag}}$,

$$\hat{H}_{\mathrm{Diag}} = \sum_{j,m} J^{s}_{x}(\hat{a}^{\dagger}_{j+1,m+1}\hat{a}_{j,m} + \mathrm{H.c.}). \tag{17}$$

Next, the next-nearest-neighbor hoppings, like the nearest-neighbor hoppings, come in two forms. The reason for both nearest- and next-nearest-neighbor hoppings is the "skewed" nature of the synthetic-dimensional brick-wall lattice caused by the linear tilt. The first type of next-nearest-neighbor hopping is, in fact, a simple hopping to an adjacent internal state with no change in the physical site, as was previously touched on. The second is a more involved next-nearest-neighbor tunneling in real space accompanied by a change in internal state, which we will refer to as a "long-diagonal" process (see Fig. 9, where purple arrows represent the long-diagonal process and red arrows represent a straightforward internal state change). As with the other hopping processes, these may be achieved by Raman-assisted tunneling by selecting a suitable Raman frequency in relation to the energy difference between the coupled states and an ancillary state, which will be another internal state along the synthetic dimension. The integrals responsible for the hopping rates associated with these tunnelings will be discussed in more depth at the end of this section. We denote them as the "purely synthetic" transition with Hamiltonian $\hat{H}_{\mathrm{Syn.}}$ and the long-diagonal transition with $\hat{H}_{\mathrm{Long}}$:

$$\hat{H}_{\mathrm{Syn.}} = \sum_{m} J^{s}(e^{i\phi j}\hat{a}^{\dagger}_{j,m+1}\hat{a}_{j,m} + \mathrm{H.c.}), \tag{18}$$

$$\hat{H}_{\mathrm{Long}} = \sum_{j,m} J^{s}_{xx}(e^{i\phi(j+2)}\hat{a}^{\dagger}_{j+2,m+1}\hat{a}_{j,m} + \mathrm{H.c.}). \tag{19}$$

Adding these terms and (17) to (16), we obtain

$$\begin{aligned}\hat{H}_{\mathrm{TB}} = \sum_{j,m}[&(\epsilon_j + aFj)\hat{a}^{\dagger}_{j,m}\hat{a}_{j,m} \\ &+ J_x(\hat{a}^{\dagger}_{j,m}\hat{a}_{j+1,m} + \hat{a}^{\dagger}_{j+1,m}\hat{a}_{j,m}) \\ &+ J^{s}(e^{i\phi j}\hat{a}^{\dagger}_{j,m+1}\hat{a}_{j,m} + e^{-i\phi j}\hat{a}^{\dagger}_{j,m}\hat{a}_{j,m+1}) \\ &+ J^{s}_{x}(\hat{a}^{\dagger}_{j+1,m+1}\hat{a}_{j,m} + \hat{a}^{\dagger}_{j,m}\hat{a}_{j+1,m+1}) \\ &+ J^{s}_{xx}(e^{i\phi(j+2)}\hat{a}^{\dagger}_{j+2,m+1}\hat{a}_{j,m} + \mathrm{H.c.})].\end{aligned} \tag{20}$$

It should be noted that purely real-space complex next-nearest-neighbor couplings can be achieved by an additional pair of laser beams and could be added here, but as discussed in Sec. II, they are unnecessary to see nontrivial topological responses. Tuning the hopping integrals such that $J_x = J^{s}_{x} = t_1$ and $J^{s} = J^{s}_{xx} = t_2$, identifying nearest neighbors and next-nearest neighbors, one may reduce Eq. (20) to

$$\begin{aligned}\hat{H}_{\mathrm{TB}} = \sum_{\mathbf{n}}(-1)^{j}\frac{U}{2}\hat{a}^{\dagger}_{\mathbf{n}}\hat{a}_{\mathbf{n}} &+ \sum_{\langle\mathbf{n},\mathbf{n}'\rangle} t_1(\hat{a}^{\dagger}_{\mathbf{n}}\hat{a}_{\mathbf{n}'} + \hat{a}^{\dagger}_{\mathbf{n}'}\hat{a}_{\mathbf{n}}) \\ &+ \sum_{\langle\langle\mathbf{n},\mathbf{n}'\rangle\rangle} t_2(e^{i\phi}\hat{a}^{\dagger}_{\mathbf{n}}\hat{a}_{\mathbf{n}'} + e^{-i\phi}\hat{a}^{\dagger}_{\mathbf{n}'}\hat{a}_{\mathbf{n}}),\end{aligned} \tag{21}$$

where t_1 and t_2 are the nearest-neighbor and next-nearest-neighbor hoppings rates, respectively. They directly correspond to the tunneling coefficients in the target Hamiltonian, Eq. (2), as does the phase ϕ. We have introduced the notation of vector indices $\mathbf{n} = (j,m)$ and $\mathbf{n}' = (j',m')$, where j indicate real-space site occupation and m indicate the internal state. We also adopt the notation $\langle\mathbf{n},\mathbf{n}'\rangle$ to signify summation over nearest neighbors [the second and fourth lines in (20)] and $\langle\langle\mathbf{n},\mathbf{n}'\rangle\rangle$ to signify summation over next-nearest neighbors [third and fifth lines in (20)]. The energy $E + V + U/2$ is an energy shift experienced by all atoms and therefore may be dropped, leaving behind only the sublattice symmetry-breaking energy $U/2$, which alternates between positive and negative on adjacent sites.

We have dropped the index in the exponential which creates a position-dependent phase gain. That is because in an experiment, all observables are a result of a local complex hopping phase creating a flux through a plaquette, keeping in mind that a phase is not globally measurable anyway. Using our proposal with position-dependent phase, it is therefore sufficient to create a tunable flux through a plaquette as in the Haldane model.

Now, the on-site energy is purely the site-dependent term, and we identify $M = U/2$ to be in agreement with [1]. Separating the site operators into those for the A and B sites to

allow for spinorial notation, we can then write

$$\begin{aligned}\hat{H} = &\sum_{\mathbf{n}} M[\hat{\psi}^{\dagger}_{\mathbf{n},A}\hat{\psi}_{\mathbf{n},A} - \hat{\psi}^{\dagger}_{\mathbf{n},B}\hat{\psi}_{\mathbf{n},B}] \\ &+ \sum_{\langle \mathbf{n},\mathbf{n}'\rangle} t_1[\hat{\psi}^{\dagger}_{\mathbf{n},B}\hat{\psi}_{\mathbf{n}',A} + \hat{\psi}^{\dagger}_{\mathbf{n}',A}\hat{\psi}_{\mathbf{n},B}] \\ &+ \sum_{\langle\langle \mathbf{n},\mathbf{n}'\rangle\rangle} t_2[e^{i\phi}\hat{\psi}^{\dagger}_{\mathbf{n},A}\hat{\psi}_{\mathbf{n}',A} + e^{-i\phi}\hat{\psi}^{\dagger}_{\mathbf{n}',A}\hat{\psi}_{\mathbf{n},A}] \\ &+ \sum_{\langle\langle \mathbf{n},\mathbf{n}'\rangle\rangle} t_2[e^{i\phi}\hat{\psi}^{\dagger}_{\mathbf{n},B}\hat{\psi}_{\mathbf{n}',B} + e^{-i\phi}\hat{\psi}^{\dagger}_{\mathbf{n}',B}\hat{\psi}_{\mathbf{n},B}]. \end{aligned} \tag{22}$$

We have dropped the tilt term since now an atom at $\mathbf{n}$ coupled to photons from a Raman laser is degenerate with the atom in the site to which the Raman beams induce a transition. This argument is from [11]. Put another way, we may drop the tilt term because we have taken this energy difference into account in the Raman scheme. Fourier transforming Eq. (22) changes it into the form of the Bloch Hamiltonian of the Haldane model as in Eq. (1) with Hamiltonian density Equation (2). This is the target Hamiltonian, and hence, we end our derivation here.

B. Energy hierarchy

Several restrictions on energies exist, creating a hierarchy of energy scales for the proposal, and they are similar to those for the Harper-Hofstadter model [27]. For example, the tilt of the potential must be greater than the bare tunneling coefficient J to inhibit this natural tunneling, as was discussed at the start of this section. The tilt, however, must be less than the energy required to excite a state of the Wannier-Stark model. This energy is the band gap of the Wannier-Stark model, which we denote ω. This restriction is in place is to prevent an atom in the ground state from tunneling to an adjacent site and occupying an excited state in that site; hence, we require $J < F < \omega$. As per [1], to ensure the bands of the energy spectrum do not overlap, the ratio of the next-nearest-neighbor tunneling coefficient to that of the nearest neighbor should fulfill $|t_2| < |t_1|/3$.

Due to the tilt and the superlattice, two distinct energy offsets, $\Delta_{\pm} = F \pm M$, exist between adjacent sites depending on whether tunneling, only along one direction, from A to B or B to A. The hierarchy is therefore modified to $J < \Delta_- \leqslant \Delta_+ < \omega$. Furthermore, if one wishes to see a topological structure, then the energy offset is required to be such that $M < 2\sqrt{3}t_2 \sin(\phi)$. This is for the four-next-nearest-neighbor case, and the argument as to the origin of this inequality is the same as discussed in Sec. II for the location of the phase transitions.

C. Next-nearest-neighbor tunneling phases

We will now discuss in more depth the Raman processes for the purely synthetic and long-diagonal hoppings. These correspond to the terms with hopping coefficients J^s and J^s_{xx} in Eq. (20), respectively. The hopping integrals leading to these coefficients are explicitly shown, as are the phases which are required to accompany these hoppings.

1. Synthetic dimension transitions

The phase which should be imprinted for the two different next-nearest-neighbor transitions needs to be carefully chosen. For the purely synthetic transition a phase of ϕ should be used. This can be tuned using the momentum transfer, which for this Raman process we denote by q_s, of the Raman beam, which is varied by changing the angle of incidence of the beam. The tunneling rate for such a transition is given by [27]

$$t_j = \Omega e^{-ijq_s}\int dx\ |W_0(x)|^2 e^{-iq_s x}. \tag{23}$$

This leads to a phase gain of e^{-ijq_s}, where j denotes the optical lattice site that the atom left. When an atom makes the transitions

$$(j,m) \to (j,m+1) \to (j+1,m+1) \to (j+1,m),$$

there is an overall phase gain given by $-\phi j - (-\phi)(j+1) = \phi$, or equivalently, there is a synthetic magnetic flux of ϕ through every plaquette. This is not too dissimilar from the two-dimensional real lattice with an effective magnetic field realized in Ref. [28], demonstrating that high effective field strengths can be attained. See [10,28,29] for technical details.

2. Long-diagonal transitions

For the other next-nearest-neighbor hopping, a long-diagonal process of two real-space hoppings and an internal level change, the required phase is $\phi/3$. When an atom makes the transitions

$$(j,m) \to (j+2,m+1) \to (j+3,m+1) \to (j+1,m),$$

there is an overall phase gain given by $-\frac{1}{3}\phi j - (-\frac{1}{3}\phi)(j+3) = \phi$. Again, here, for long-diagonal processes, there is an equivalent magnetic flux ϕ piercing the plaquette.

The tunneling rate for such a transition is given by [27]

$$t_{j\to j+2} = \Omega e^{-ijq_x}\int dx\ W_0(x)W_2(x)e^{-iq_x x}. \tag{24}$$

The number of lasers may be reduced if the required frequency, polarization, and intensity of any two coincide. As discussed for the triangular lattice in Ref. [26], three tunnelings may be created from three lasers, where a Raman process usually involves two laser beams.

To increase the synthetic dimension length, more states from the hyperfine manifold must be coupled together. The spacing in energy may not always be the same between any two adjacent sites; hence, the Rabi frequencies need to be adjusted according to Clebsch-Gordan coefficients. The energy spacings are given by $\Omega g_{F,m}$, with

$$g_{F,m} = \sqrt{F(F+1) - m(m+1)}, \tag{25}$$

where F denotes the angular momentum quantum number and m denotes its projection. For alkali metals it has been noted that these modifications are not negligible (for example, see the Supplemental Material of [13]). This means that for every "ribbon" of synthetic dimension one wishes to include in the lattice, extra lasers coupling the extra internal states may be required.

One would imagine that a minimum of three internal m states are required: The "largest" internal state, hosting an

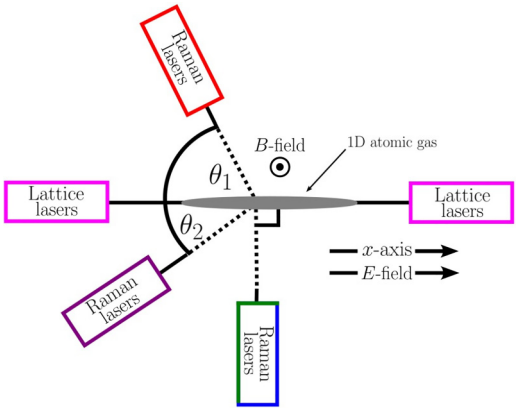

FIG. 10. Angles are for demonstrative purposes only. Magnetic field is out of the page, and electric fields is along x, as indicated. Pink-boxed lasers (left- and rightmost) generate the superlattice. The green-and-blue-boxed laser (bottommost) creates nearest-neighbor hoppings, while the red-boxed- (topmost) and purple-boxed (bottom left) lasers induce next-nearest-neighbor hoppings.

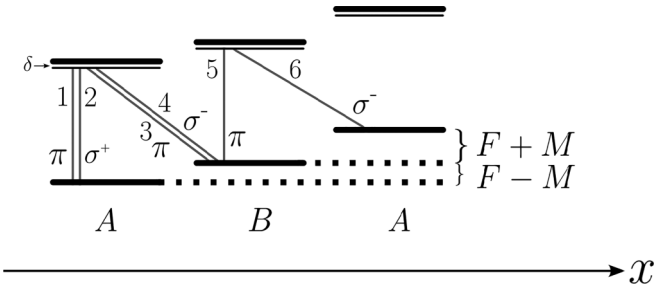

FIG. 11. Laser beam configuration for couplings, demonstrated with ancillary states, which are adjacent states along the synthetic dimension. Transitions are labeled by numbers 1 through 6. Here, π, σ^+, and σ^- indicate the polarization, and δ is the detuning. Beams 1 and 2 create purely synthetic transitions, beams 1 and 3 create spatial tunneling, and beams 1 and 4 create diagonal tunneling. Beams 5 and 6 are the additional pair of laser beams introduced to cancel out every other diagonal tunneling provided the complex phase of this process is greater than the complex phase of the beam process of beams 1 and 3 by π.

edge state with one direction of propagation; the "smallest" internal state, hosting an edge state with a current flow opposite to that of the largest state; and, sandwiched between them, an internal state which has minimal particle transport. This was the case for the quantum-Hall-effect synthetic-dimension experiments [3,4]. Alkaline-earth and alkaline-earth-like atoms demonstrate SU(N)-invariant interactions, meaning that the effects of spin-changing collisions are suppressed [30]. If one uses a three-legged ladder, due to the small number of internal states used, the edge states will be relatively more populated, which would facilitate spin-selective imaging. Hence, there is a payoff between observing states from deep within the bulk and sufficiently populated edge states [3]. Finite-size effects in synthetic dimensions are nontrivial and were considered previously for the Harper-Hofstadter model, for which it was shown that a topological signature may still be extracted [31].

IV. RAMAN SCHEME

An experimental setup to realize the Haldane model in a synthetic-dimensional system could be as follows. First, two sets of counterpropagating laser beams create the superlattice, and an electric field applied along the x axis induces the linear tilt F to create the potential in Eq. (9). These are represented by the pink-boxed lasers in Fig. 10. An atomic gas is trapped using harmonic traps to create a quasi-one-dimensional gas sample. In the physical y and z directions we require tight confinement. Next, a magnetic field is applied to the sample to create Zeeman splitting between the energies of the internal states of the hyperfine manifold. The synthetic-dimensional brick-wall lattice is formed by the green-and-blue-boxed Raman lasers in Fig. 10, which correspond to the green and blue arrows in Fig. 8; that is, these lasers are responsible for nearest-neighbor hopping. The Raman process is as illustrated in Fig. 11 and bears a resemblance to double-λ schemes, as used in laser spectroscopy setups [32]. As an example, say that beam 1 has a one-photon Rabi frequency of Ω_{12} and beam 2 has a frequency of Ω_{23}, with a detuning of δ to the ancillary state 2; then the rate at which this process would occur is dependent on the two-photon Rabi frequency Ω given by (15), as well as a factor due to the overlap of the Wannier functions, and a complex phase due to the angle of incidence of the beams. This is per Eq. (23).

The recoil momentum imparted on an atom, which leads to a complex argument in the hopping integral, is given by

$$k_R = \frac{2\pi\,\cos\theta}{\lambda_R}, \tag{26}$$

where θ is the angle of incidence of the beam and λ_R is its wavelength. Since nearest-neighbor hoppings are entirely real, the angle of incidence for the green-and-blue-boxed lasers is orthogonal to the x axis.

Finally, next-nearest-neighbor hoppings are added through the inclusion of two more Raman lasers, the purple-boxed and red-boxed lasers in Fig. 10, corresponding to the purple and red hoppings in Fig. 9. The angles of incidence for these two lasers must be precisely selected. They are labeled by θ_1 and θ_2 for the purely synthetic and long-diagonal hoppings, respectively, in Fig. 10. As mentioned in Sec. III C, the two hoppings require two different complex arguments. Labeling the wavelength of the red-boxed laser as λ_1 and that of the purple-boxed laser as λ_2, the two angles are given by

$$q^s = \phi = \frac{2\pi\,\cos\theta_1}{\lambda_1}, \tag{27}$$

$$q^s_{xx} = \frac{\phi}{3} = \frac{2\pi\,\cos\theta_2}{\lambda_2}, \tag{28}$$

and hence, they are related to one another by the following two equivalent equations:

$$\frac{\cos\theta_1}{\lambda_1} = \frac{3\cos\theta_2}{\lambda_2}, \tag{29}$$

$$\theta_1 = \cos^{-1}\left(\frac{3\lambda_1}{\lambda_2}\cos\theta_2\right). \tag{30}$$

Hence, if θ_2 is changed, then θ_1 needs to be changed according to (30). The purely synthetic transition can also be seen in

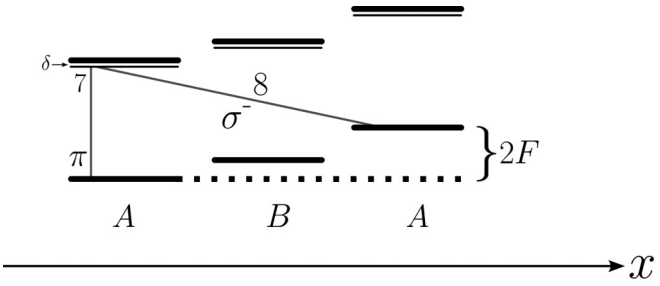

FIG. 12. The next-nearest-neighbor long-diagonal coupling λ or Raman scheme. As discussed in the text, if beam 7 matches any of the beams from Fig. 11, then the number of beams may be reduced.

Fig. 11. The Raman scheme for the remaining next-nearest-neighbor hopping, the long-diagonal tunneling, can be seen in Fig. 12.

As mentioned in Sec. III C, the inclusion of additional internal states would require additional lasers. The hopping integrals must all be the same; otherwise, the notion of a Brillouin zone is not well defined. Hence, these lasers may have distinct wavelengths and so will have their own unique angles of incidence, as given by (26).

Depending on energy scales, there may exist another option for removing alternating diagonal hoppings. A nearest-neighbor hopping in the x direction from site A to B is due to a Raman process with specific one-photon Rabi frequencies and detuning. Provided that all these energy scales are distinct enough from the process which takes one from site B to A, then this transition should not take place.

A larger-frequency detuning of the Raman beams was found to produce fewer unwanted heating effects [11]. Tunneling rates of at least 1 Hz are required for experimental implementations of models involving next-nearest-neighbor atoms [11], and this is achievable thanks to Raman-assisted tunneling, as the bare tunneling may be much smaller than this rate. Furthermore, an advantage of using Raman-assisted tunneling is that nearest-neighbor and next-nearest-neighbor tunneling rates can be controlled independently. The first experimental realization of the Haldane model achieved next-nearest tunneling rates of 5 and 18 Hz. This was done by way of an elliptically modulated honeycomblike lattice, giving rise to an effective Hamiltonian with complex next-nearest-neighbor couplings which the ^{40}K atoms experience (see [2], in particular, the "Methods" section and the Supplementary Materials).

V. EDGE STATES

A good starting point for considering edge states in our proposal is the experimental realizations of the quantum Hall effect in synthetic dimensions. Using a three-leg lattice in a quantum Hall regime [3,4], time-of-flight methods were used to obtain the lattice momentum distribution $n(k)$ by a series of spin-selective images, tracking the expansion of the atomic cloud. Next, the lattice momentum imbalance, a quantification of the asymmetry in the momentum distribution for a leg m, is given by

$$\mathcal{I}_m = \int_0^{\frac{\pi}{a}} dk_x \, [n_m(k_x) - n_m(-k_x)]; \tag{31}$$

the values for the top and bottom legs of the lattice (for example, $m = \pm 1$ in Ref. [4]) were found to be equal and opposite, while for the central leg ($m = 0$ [4]) the value was found to be close to zero. In our proposal, the direction of the edge-state propagation depends on the phase. That is, there are two different situations depending on whether $\phi \in (0, \pi)$ or $\phi \in (\pi, 2\pi)$. Furthermore, in Ref. [4], with the use of quench dynamic experiments, the classic cyclotron motion was observed, giving a skipping effect along the boundary, as expected. In our proposal, the edge states are located on an edge which corresponds to the zigzag edge. To realize an armchair edge, one would need to exchange the synthetic and real dimensions, which would most likely require highly involved, spin-dependent, and site-dependent tunneling. Edge states on armchair lattices, however, are only thought to exist in the presence of anisotropy [33].

VI. INTERACTIONS

Considered separately, the topics of interactions in synthetic dimensions and in topological systems are fascinating problems. In synthetic-dimensional systems, interactions which take place between atoms, where the internal state of the atom is the extra dimension, may give rise to nonlocal effects since the atoms can reside in the same physical site but be separated in the synthetic dimension.

For example, consider all the atoms on the same site in Fig. 9 and notice they are "linked" to one another by the red arrows, which represent the purely synthetic-dimensional hopping discussed in Sec. III C. Considering what arrows these would be in the brick-wall lattice with the aid of Fig. 1(b), we realize that they are *next*-nearest-neighbor hoppings, and so interactions would take place in the brick-wall lattice *only* along some axis at an angle $\frac{\pi}{4}$ with respect to the lattice vectors. Thus, interactions in the synthetic dimensions would simulate highly anisotropic interactions in the original model.

Although we may wish to suppress the effects of interactions, we note in passing that interactions are extremely important in other situations. Interactions between electrons are seemingly a prerequisite for the appearance of the fractional quantum Hall effect [34]. In a similar vein, interactions have been considered as a route to fractionalization in ultracold-atom systems too, by way of charge pumping [35]. The infinite range interaction found along a synthetic dimension is a large obstacle which needs to be circumvented to realize a fractional Chern insulator in such a system. These problematic interactions may be made short range by way of Trotterization of the system [36] and therefore provide a basis for fractional excitations in synthetic dimensions. Taking a different route, by coupling the top- and bottommost legs of the synthetic ladder and reinterpreting the system as a cylinder, it was shown that fractional quantum Hall states in the form of density waves can arise [37].

Coherent collisions in spin-1 Bose-Einstein condensates have been studied to the extent that they have even been experimentally exploited to determine the spin-dependent scattering length [38]. In this instance, the internal dynamics are decoupled from the spatial macroscopic wave function as the spin healing length is larger than the size of the condensate.

Ideally, spin-changing collisions would be suppressed, or population dynamics would average nicely to allow for the extraction of topological signatures.

The Chern number classifies the topology of a gapped band structure for a noninteracting system, and so two bands with the same Chern number may be deformed into each other without closing the gap and changing any properties. First, we will discuss the spinless case. Weak interactions in the Haldane model have little effect on the system [24]. However, for repulsive nearest-neighbor interactions of the same order of magnitude as nearest-neighbor hopping, the topological phases are destroyed, and a charge-density-wave insulating state appears [39]. Expanding on this work, it was determined that adding on-site disorder interactions and varying the strengths of the two different types of interactions can give rise to different types of insulating states depending on the relative strengths of the interactions [40].

An *attractive* Hubbard interaction, which is, again, infinite along the synthetic dimension, was shown to induce Cooper pairing between the counterpropagating chiral edge states in quantum Hall ribbons [3,4], leading to a one-dimensional topological superfluid exhibiting Majorana physics [41]. Furthermore, exotic states of matter such as the supersolid are found in synthetic models with interactions. For example, for a bipartite lattice inhabited by internally coupled atoms with next-nearest-neighbor hopping, at low tunneling rates, there exist a charge density wave at exactly half filling, a supersolid on one sublattice below this filling fraction, and phase separation above this filling fraction. At high next-nearest-neighbor tunneling rates, there exists a phase which is dominated by superfluid order [42]. Hence, one needs to be careful that one is sufficiently far away from this regime if one wishes to use a bipartite superlattice in a cold-atom experiment.

In summary, the inclusion of interactions affects the order of the quantum fluid and will therefore have an effect on the model the quantum fluid is simulating.

VII. CONCLUSION

We outlined a proposal for a semisynthetic-dimensional realization of the Haldane model. Our scheme exploits the fact that the brick-wall lattice is topologically equivalent to the honeycomb lattice. By first realizing this in a synthetic fashion using an optical lattice and coupled internal states of an atom, one may go on to realize the Haldane model. This is done through the introduction of complex next-nearest-neighbor hopping terms via Raman-assisted tunneling and by making the lattice bipartite. The flux through a plaquette of the lattice can be changed by varying the angle of incidence of the Raman beams. One can additionally change the energy offset between adjacent sites of the optical superlattice, giving experimental access to the full range of parameters required to explore the phase diagram of the model. Our proposal could be a new platform for the investigation of topologically nontrivial materials. For example, one could extend the model into the x-y plane where each row of sites displays this model. Coupling this system to a copy of itself would emulate a bilayer Haldane model, which is an interesting problem to consider [43].

When the energy spectrum exhibits no band gap, for example, at $\phi = \frac{\pi}{2}$ and $M = 2\sqrt{3}\,t_2$, the system is referred to as a topological semimetal, which may have a nontrivial winding number if the Fermi energy is such that the lower band is filled [44]. Our proposal may allow for the realization of such states of matter; however, the origin of this phase is subtle, as it is due to the laser recoil momentum, which is not a feature of the original Haldane model. The analogous situation with regard to synthetic dimensions is an open question.

The quantum Hall effect was more recently reproduced in cold-atom systems with a larger bulk. This was done by including more states of the hyperfine manifold, effectively adding more sites along the synthetic dimension. A regime coupling six internal states was achieved with the species ^{168}Er [45], and a regime of 11 states was achieved with the species ^{162}Dy [46]. Although we mentioned that coupling three states is the most attainable, these experiments indicate that our scheme may be extended to include internal states with a synthetic dimension numbering five, six, or even greater.

ACKNOWLEDGMENTS

The authors acknowledge helpful discussions with S. Lang. J.P. acknowledges financial support from an EPSRC DTP Scholarship, and G.V.-R. acknowledges financial support from EPSRC CM-CDT Grant No. EP/L015110/1.

[1] F. D. M. Haldane, Phys. Rev. Lett. **61**, 2015 (1988).
[2] G. Jotzu, M. Messer, R. Desbuquois, M. Lebrat, T. Uehlinger, D. Greif, and T. Esslinger, Nature (London) **515**, 237 (2014).
[3] M. Mancini *et al.*, Science **349**, 1510 (2015).
[4] B. K. Stuhl, H.-I. Lu, L. M. Aycock, D. Genkina, and I. B. Spielman, Science **349**, 1514 (2015).
[5] O. Boada, A. Celi, J. I. Latorre, and M. Lewenstein, Phys. Rev. Lett. **108**, 133001 (2012).
[6] H. M. Price, O. Zilberberg, T. Ozawa, I. Carusotto, and N. Goldman, Phys. Rev. Lett. **115**, 195303 (2015).
[7] I. Petrides, H. M. Price, and O. Zilberberg, Phys. Rev. B **98**, 125431 (2018).
[8] C. H. Lee, Y. Wang, Y. Chen, and X. Zhang, Phys. Rev. B **98**, 094434 (2018).
[9] J. Jünemann, A. Piga, S.-J. Ran, M. Lewenstein, M. Rizzi, and A. Bermudez, Phys. Rev. X **7**, 031057 (2017).
[10] M. Aidelsburger, M. Atala, M. Lohse, J. T. Barreiro, B. Paredes, and I. Bloch, Phys. Rev. Lett. **111**, 185301 (2013).
[11] H. Miyake, G. A. Siviloglou, C. J. Kennedy, W. C. Burton, and W. Ketterle, Phys. Rev. Lett. **111**, 185302 (2013).
[12] S. Greschner and L. Santos, Phys. Rev. Lett. **115**, 053002 (2015).
[13] A. Celi, P. Massignan, J. Ruseckas, N. Goldman, I. B. Spielman, G. Juzeliūnas, and M. Lewenstein, Phys. Rev. Lett. **112**, 043001 (2014).

[14] M. Buchhold, D. Cocks, and W. Hofstetter, Phys. Rev. A **85**, 063614 (2012).
[15] T. D. Stanescu, V. Galitski, J. Y. Vaishnav, C. W. Clark, and S. Das Sarma, Phys. Rev. A **79**, 053639 (2009).
[16] C. Braun, R. Saint-Jalm, A. Hesse, J. Arceri, I. Bloch, and M. Aidelsburger, arXiv:2304.01980.
[17] Y. Hatsugai, Solid State Commun. **149**, 1061 (2009).
[18] P. Delplace, D. Ullmo, and G. Montambaux, Phys. Rev. B **84**, 195452 (2011).
[19] N. Hao, P. Zhang, Z. Wang, W. Zhang, and Y. Wang, Phys. Rev. B **78**, 075438 (2008).
[20] M. C. Rechtsman, J. M. Zeuner, Y. Plotnik, Y. Lumer, D. Podolsky, F. Dreisow, S. Nolte, M. Segev, and A. Szameit, Nature (London) **496**, 196 (2013).
[21] Y. Kuno, I. Ichinose, and Y. Takahashi, Sci. Rep. **8**, 10699 (2018).
[22] S.-L. Zhu, L.-B. Shao, Z. D. Wang, and L.-M. Duan, Phys. Rev. Lett. **106**, 100404 (2011).
[23] M. F. Maghrebi, S. Ganeshan, D. J. Clarke, A. V. Gorshkov, and J. D. Sau, Phys. Rev. Lett. **115**, 065301 (2015).
[24] M. Z. Hasan and C. L. Kane, Rev. Mod. Phys. **82**, 3045 (2010).
[25] M. C. Rechtsman, Y. Plotnik, J. M. Zeuner, D. Song, Z. Chen, A. Szameit, and M. Segev, Phys. Rev. Lett. **111**, 103901 (2013).
[26] D. Suszalski and J. Zakrzewski, Phys. Rev. A **94**, 033602 (2016).
[27] H. Miyake, Ph.D. thesis, Massachusetts Institute of Technology, 2013.
[28] M. Aidelsburger, M. Atala, S. Nascimbène, S. Trotzky, Y.-A. Chen, and I. Bloch, Phys. Rev. Lett. **107**, 255301 (2011).
[29] M. Atala, M. Aidelsburger, M. Lohse, J. T. Barreiro, B. Paredes, and I. Bloch, Nat. Phys. **10**, 588 (2014).
[30] G. Pagano *et al.*, Nat. Phys. **10**, 198 (2014).
[31] D. Genkina, L. M. Aycock, H.-I. Lu, M. Lu, A. M. Pineiro, and I. B. Spielman, New J. Phys. **21**, 053021 (2019).
[32] T. Zanon, S. Guerandel, E. de Clercq, D. Holleville, N. Dimarcq, and A. Clairon, Phys. Rev. Lett. **94**, 193002 (2005).
[33] M. Kohmoto and Y. Hasegawa, Phys. Rev. B **76**, 205402 (2007).
[34] D. E. Feldman and B. I. Halperin, Rep. Prog. Phys. **84**, 076501 (2021).
[35] T.-S. Zeng, C. Wang, and H. Zhai, Phys. Rev. Lett. **115**, 095302 (2015).
[36] L. Barbiero, L. Chomaz, S. Nascimbene, and N. Goldman, Phys. Rev. Res. **2**, 043340 (2020).
[37] S. Barbarino, L. Taddia, D. Rossini, L. Mazza, and R. Fazio, Nat. Commun. **6**, 8134 (2015).
[38] M.-S. Chang, Q. Qin, W. Zhang, L. You, and M. S. Chapman, Nat. Phys. **1**, 111 (2005).
[39] E. Alba, J. K. Pachos, and J. J. García-Ripoll, New J. Phys. **18**, 033022 (2016).
[40] T.-C. Yi, S. Hu, E. V. Castro, and R. Mondaini, Phys. Rev. B **104**, 195117 (2021).
[41] Z. Yan, S. Wan, and Z. Wan, Sci. Rep. **5**, 15927 (2015).
[42] T. Bilitewski and N. R. Cooper, Phys. Rev. A **94**, 023630 (2016).
[43] S. Bhattacharjee, S. Bandyopadhyay, D. Sen, and A. Dutta, Phys. Rev. B **103**, 224304 (2021).
[44] N. Goldman, E. Anisimovas, F. Gerbier, P. Öhberg, I. B. Spielman, and G. Juzeliūnas, New J. Phys. **15**, 013025 (2013).
[45] T. Chalopin, T. Satoor, A. Evrard, V. Makhalov, J. Dalibard, R. Lopes, and S. Mascimbene, Nat. Phys. **16**, 1017 (2020).
[46] R. V. Roell, A. W. Laskar, F. R. Huybrechts, and M. Weitz, Phys. Rev. A **107**, 043302 (2023).